A&A 389, 446–463 (2002)
DOI: 10.1051/0004-6361:20020597

Astronomy & Astrophysics

Chemistry as a probe of the structures and evolution of massive star-forming regions

S. D. Doty[1], E. F. van Dishoeck[2], F. F. S. van der Tak[2,3], and A. M. S. Boonman[2]

[1] Department of Physics and Astronomy, Denison University, Granville, OH 43023, USA
[2] Sterrewacht Leiden, PO Box 9513, 2300 RA Leiden, The Netherlands
[3] Max-Planck-Institut für Radioastronomie, Auf dem Hügel 69, 53121 Bonn, Germany

Received 31 October 2001 / Accepted 15 April 2002

Abstract. We present detailed thermal and gas-phase chemical models for the envelope of the massive star-forming region AFGL 2591. By considering both time- and space-dependent chemistry, these models are used to study both the physical structure proposed by van der Tak et al. (1999, 2000), as well as the chemical evolution of this region. The model predictions are compared with observed abundances and column densities for 29 species. The observational data cover a wide range of physical conditions within the source, but significantly probe the inner regions where interesting high-temperature chemistry may be occurring. Taking appropriate care when comparing models with both emission and absorption measurements, we find that the majority of the chemical structure can be well-explained. In particular, we find that the nitrogen and hydrocarbon chemistry can be significantly affected by temperature, with the possibility of high-temperature pathways to HCN. While we cannot determine the sulphur reservoir, the observations can be explained by models with the majority of the sulphur in CS in the cold gas, SO_2 in the warm gas, and atomic sulphur in the warmest gas. Because the model overpredicts CO_2 by a factor of 40, various high-temperature destruction mechanisms are explored, including impulsive heating events. The observed abundances of ions such as HCO^+ and N_2H^+ and the cold gas-phase production of HCN constrain the cosmic-ray ionization rate to $\sim 5.6 \times 10^{-17}$ s^{-1}, to within a factor of three. Finally, we find that the model and observations can simultaneously agree at a reasonable level and often to within a factor of three for $7 \times 10^3 \leq t(\mathrm{yrs}) \leq 5 \times 10^4$, with a strong preference for $t \sim 3 \times 10^4$ yrs since the collapse and formation of the central luminosity source.

Key words. stars: formation – stars: individual: AFGL 2591 – ISM: molecules

1. Introduction

The distribution and composition of dust and gas around isolated low-mass young stellar objects (YSOs) has been well-studied both observationally and theoretically. Unfortunately, much less is known about the distribution and composition of material around high-mass YSOs (see e.g., Churchwell 1993, 1999). The higher densities and masses, and shorter lifetimes associated with massive star formation suggest that differences between regions of high- and low-mass star formation can be expected.

Recent observational advances (e.g., submillimeter beams of $\sim 15''$ sampling smaller regions of higher critical densities, interferometry at 1 and 3 mm, and ground- and space-based infrared observations of gas and ices) have led to a new and better understanding of the environment around massive YSOs (see e.g., Garay & Lizano 1999; van Dishoeck & Hogerheijde 1999; Hatchell et al. 2000; Beuther et al. 2002). In this vein, van der Tak et al. (1999, 2000) have conducted detailed multi-wavelength studies of high-mass YSOs, and begun to form a picture for the physical structure of some of these regions. The proposed material distributions in the envelopes fit a wide variety of continuum and spectral line data. However, they are incomplete without a detailed thermal and chemical structure. The proposed material distribution can be used to test the chemical structure and evolution of the envelope, and the combined results can eventually be used to compute line strengths and profiles for direct comparison with observations.

Significant work has been involved in developing an understanding of the chemistry of star-forming regions. This ranges from studies of cold, dark clouds (e.g., Herbst & Klemperer 1973; Prasad & Huntress 1980; Leung et al. 1984; Gwenlan et al. 2000) to "hot cores" (see e.g., reviews by Millar 1993; Walmsley & Schilke 1992; Kurtz et al. 2000). In nearly all cases, however, the chemistry is considered for a homogeneous cloud, or a point within a

Send offprint requests to: S. Doty,
e-mail: doty@cc.dension.edu

cloud (see, though, Xie et al. 1995 and Bergin et al. 1995 for counter examples). Unfortunately, the physical conditions (i.e., temperature and density) vary strongly with position within the envelope, meaning that potentially extreme chemical variations may occur between the source center and the observer. It is this strong variation of chemical composition with position and time that may provide one of the best benchmarks of our understanding of both the structures and evolution of massive star-forming regions.

In this paper, we utilize position-dependent thermal balance and time- and position-dependent chemical modeling to probe the validity of the physical structures proposed by van der Tak et al. (1999 & 2000), and more importantly, to study the chemical evolution of AFGL 2591. In particular, taking their structure as a starting point, we construct detailed models for the gas-phase chemistry of this source, and compare the results with observations. AFGL 2591 is a massive ($\sim$42 $M_\odot$ within $r = 3\times10^4$ AU), luminous ($\sim 2\times10^4$ $L_\odot$) infrared source with many of the properties thought to characterize YSOs. While most massive stars form in clusters, AFGL 2591 has the advantage that it is forming in relative isolation – allowing us to study its physical, thermal, and chemical structures without influence from other nearby massive sources. It has the further advantage of being well-observed both in the continuum and in a variety of molecular lines.

This paper is organized as follows. The existing observations providing the model constraints are briefly discussed in Sect. 2. In Sect. 3, the model is described. The model is then applied to AFGL 2591 and compared with the observational results in Sect. 4. In Sect. 5, we compare our time-dependent model predictions with the observations in order to constrain the chemical age of the envelope. Finally, we summarize our results and conclude in Sect. 6.

2. Existing observations and usage

AFGL 2591 has been well-observed both in the continuum and in various molecular lines. While no new observations are presented in this paper, it is important to briefly note and discuss the relevant observations as they provide the constraints placed on the model.

2.1. Continuum

AFGL 2591 has been observed in the range 2–60 000 μm by Lada et al. (1984), Aitken (1988), Sandell (1998, private communication), and van der Tak et al. (1999). These results were analyzed by van der Tak et al. (2000 – see Sect. 3 below) to constrain the density distribution and grain properties – necessary for not only the thermal structure, but also to properly evaluate the gas thermal balance and hence obtain the gas temperature as a function of position.

2.2. Molecular lines

A wide variety of observations, both in the infrared and submillimeter, have been conducted of molecular gas in AFGL 2591, some of which are as of yet unpublished. The results are summarized in Table 1, where the species, observed abundance [$x(\mathrm{X}) \equiv n(\mathrm{X})/n(\mathrm{H_2})$] or column density [$N(\mathrm{X})$], inferred excitation temperature, method of analysis, weight used in selecting the most important of the relevant observations, type of observation, and reference are listed.

2.3. Notes on Table 1 and usage of the data

The observation type is listed in Table 1 as this is significant for comparing the results with observations. For infrared absorption lines, the molecules observed are along the (narrow) line of sight to the background continuum source. Consequently, these results should be compared to model "radial column densities", namely $N_{\mathrm{radial}} \equiv \int n(r)\mathrm{d}r$. On the other hand, submillimeter emission lines arise from throughout the envelope. In these cases, averages over the beam are used in comparing predicted and observed column densities. Here, the "beam-averaged column density" is defined as $N_{\mathrm{beam}} \equiv \iint n(z,p)\ \mathrm{d}z\ G(p)2\pi p\ \mathrm{d}p / \int G(p)2\pi p\ \mathrm{d}p$ where p is the impact parameter, and $G(p)$ is the beam response function. We also divide the data in this fashion, as we expect many of the uncertainties in the analysis to be similar for one type of observation.

In Cols. 2 and 3 of Table 1 we list the inferred fractional abundance or column density of the given molecule toward AFGL 2591. This is done to provide the most comprehensive set of information with which to compare our models.

While determination of column density is relatively straightforward for infrared absorption lines in the limit of no re-emission, the situation is more difficult for emission lines as the emission may arise from a range of radii, and thus a range of densities, temperatures, chemical abundances, and optical depths. To combat this, some effort has been made recently to determine the fractional abundance within the envelope through detailed, non local thermodynamic equilibrium (NLTE) radiative transfer (RT) modeling (van der Tak et al. 1999). When this is done, we view the inferred abundances as superior to pure column densities as they account for many of the potential errors in determining the column density. As examples, van der Tak et al. (2000) and Boonman et al. (2001) have used such modeling to suggest "jump" models for the chemical enhancement of species within certain regions of YSO envelopes. As a result, in Col. 5 we note the method used in determining the observational result. We also use these criteria to assign a weight (higher is better) in Col. 6 to denote which data/fits we view as superior. In cases where the fit due to radiative transfer modeling is only moderate, we give this result the same weight as the results from other methods.

Table 1. Inferred column densities and abundances toward AFGL 2591.

Molecule	x	N (cm^{-2})	$T_{\rm ex}$(K)	Method	Weight	Data	Ref
H_2		9.6(22)	-	Scale N(CO)	2	-	a
$HCN^{(\alpha1)}$	$\sim$1(−8)		$\lesssim$230	NLTE RT Model	3	submm - JCMT	b
$\ldots^{(\alpha2)}$	$\sim$1(−6)		$\gtrsim$230	NLTE RT Model	3	submm - JCMT	b
$HCN^{(\alpha1)}$		4.0(16)	600	Absn. Depth	2	IR - ISO	a
$HCN^{(\beta1)}$		2.0(15)	38 (CO)	Absn. Depth	2	IR - ISO	a
$\ldots^{(\beta2)}$		4.5(16)	1010 (CO)	Absn. Depth	2	IR - ISO	a
$HCN^{(\alpha1)}$		$\leq$1.7(16)	38 (CO)	Absn. Depth	2	IR - IRTF	c
$\ldots^{(\alpha2)}$		2.0(16)	200 (CO)	Absn. Depth	2	IR - IRTF	c
$\ldots^{(\alpha3)}$		1.6(16)	1010 (CO)	Absn. Depth	2	IR - IRTF	c
$HNC^{(\alpha1)}$		2.9(13)	-	NLTE / escape prob.	2	submm - JCMT	d
$HNC^{(\alpha1)}$	1.0(−8)		-	NLTE RT Model	3	submm - JCMT	n
$HC_3N^{(\alpha1)}$		5.0(12)	-	NLTE / escape prob.	2	submm - JCMT or CSO	d
$HC_3N^{(\alpha1)}$	2.0(−8)		-	NLTE RT Model	2	submm - JCMT	n
$HCO^{+(\alpha1)}$	1.0(−8)		-	NLTE RT Model	3	submm - JCMT	e
$HCS^{+(\alpha1)}$	3.0(−10)		-	NLTE RT Model	3	submm - JCMT	n
$H_3^{+(\alpha1)}$		2 − 3(14)	-	Absn. Depth	2	IR - UKIRT	f
$H_2O^{(\alpha1)}$		3.5(18)	450	Absn. Depth	2	IR - ISO	g
$H_2S^{(\alpha1)}$		$\leq$1.0(19)	-	Absn. Depth	2	IR - ISO	h
$H_2CO^{(\alpha1)}$	2.0(−9)		-	NLTE RT Model	3	submm - JCMT	i
$H_2CO^{(\beta1)}$		8.0(13)	89	LTE Rot. Diagram	2	submm - JCMT	e
$H_2CS^{(\alpha1)}$	1.0(−9)		-	NLTE RT Model	2	submm - JCMT	n
$CI^{(\alpha1)}$		$\leq$6.8(17)	-	NLTE / escape prob.	2	submm - CSO	j
$C^{+(\alpha1)}$		$\leq$6.8(17)	-	LTE escape prob.	2	IR - ISO	k
$C_2H^{(\alpha1)}$	2.0(−9)		-	NLTE RT Model	3	submm - JCMT	n
$C_2H_2^{(\alpha1)}$		$\leq$2.0(16)	900	Absn. Depth	2	IR - ISO	a
$C_2H_2^{(\beta1)}$		$\leq$1.0(15)	38 (CO)	Absn. Depth	2	IR - ISO	a
$\ldots^{(\beta2)}$		2.0(16)	1010 (CO)	Absn. Depth	2	IR - ISO	a
$C_2H_2^{(\alpha1)}$		$\leq$8.0(14)	38 (CO)	Absn. Depth	2	IR - IRTF	c
$\ldots^{(\alpha2)}$		4.2(15)	200 (CO)	Absn. Depth	2	IR - IRTF	c
$\ldots^{(\alpha3)}$		1.0(16)	1010 (CO)	Absn. Depth	2	IR - IRTF	c
$CH_4^{(\alpha1)}$		2.5(17)	$\geq$1000	Absn. Depth	2	IR - ISO	h
$CH_4^{(\alpha1)}$		$\leq$8.0(15)	38 (CO)	Absn. Depth	2	IR - IRTF	c
$\ldots^{(\alpha2)}$		$\leq$1.0(17)	200 (CO)	Absn. Depth	2	IR - IRTF	c
$\ldots^{(\alpha3)}$		$\leq$1.3(18)	1010 (CO)	Absn. Depth	2	IR - IRTF	c
$CH_3OH^{(\alpha1)}$	2.6(−9)		$\leq$90	NLTE RT Model	3	submm - JCMT	i
$\ldots^{(\alpha2)}$	8.0(−8)		$\geq$90	NLTE RT Model	3	submm - JCMT	i
$CH_3OH^{(\beta1)}$		1.2(15)	163	rot. diagram	2	submm - JCMT	i
$CH_3CN^{(\alpha1)}$	2.0(−8)		-	NLTE RT Model	2	submm - JCMT	n

In both cases, where an excitation temperature can be assigned to the data, we note the temperature for that component as $T_{\rm ex}$ in Col. 4 of Table 1. While $T_{\rm ex}$ is not necessarily equal to the kinetic temperature, it does give some indication as to the region from which the observation arises. The values of 38, 200 and 1010 K refer to the excitation temperatures of CO found by Mitchell et al. (1989) in infrared absorption line studies. The 200 K component is thought to be associated with shocked outflowing material, whereas the other two temperatures refer to the quiescent envelope.

Finally, we note the relative importance of different measurements for probing various regions in the envelope. Absorption is confined to the narrow line of sight toward the central source. For centrally-condensed envelopes, the column density is dominated by the interior. This makes absorption measurements useful for probing the warm interior. On the other hand, emission measurements can and often do arise from throughout the envelope. When the density falls off slower than r^{-2} as is the case for AFGL 2591 (van der Tak et al. 1999) the outer portion of the envelope dominates the mass, and so emission

Table 1. continued.

Molecule	x	N (cm^{-2})	$T_{\rm ex}$(K)	Method	Weight	Data	Ref
$CO^{(\alpha1)}$		1.3(19)	-	Absn. Depth	2	IR - CFHT	o
$CO^{(\alpha1)}$		3.4(19)	-	NLTE RT Model	3	submm - JCMT	e
$CO_2^{(\alpha1)}$		2.5(16)	500	Absn. Depth	2	IR - ISO	g
$CS^{(\alpha1)}$	3.0(−9)		40	NLTE RT Model	3	submm - JCMT	e
$CS^{(\alpha1)}$		≤2.6(15)	38 (CO)	Absn. Depth	2	IR - IRTF	c
$\ldots^{(\alpha2)}$		≤3.4(15)	200 (CO)	Absn. Depth	2	IR - IRTF	c
$\ldots^{(\alpha3)}$		≤9.0(15)	1010 (CO)	Absn. Depth	2	IR - IRTF	c
$CN^{(\alpha1)}$	5.0(−8)		-	NLTE RT Model	2	submm - JCMT	n
$OH^{(\alpha1)}$		≥4.7(14)	-	Absn. Depth	2	IR - ISO	h
$O_2^{(\alpha1)}$	≤1.0(−6)		-	NLTE / opt. thin	3	submm - SWAS	l
$OCS^{(\alpha1)}$		1.0(14)	-	NLTE / escape prob.	2	submm - JCMT	d
$OCS^{(\alpha1)}$	4.0(−8)		-	NLTE RT Model	3	submm - JCMT	n
$NH_3^{(\alpha1)}$		≤5.0(14)	38 (CO)	Absn. Depth	2	IR - IRTF	c
$\ldots^{(\alpha2)}$		≤1.0(15)	200 (CO)	Absn. Depth	2	IR - IRTF	c
$\ldots^{(\alpha3)}$		≤7.0(15)	1010 (CO)	Absn. Depth	2	IR - IRTF	c
$NH_3^{(\alpha1)}$	2.0(−8)		-	NLTE RT Model	2	cm - Effelsberg	n
$N_2H^{+(\alpha1)}$		1.4(12)	-	NLTE / escape prob.	2	submm - JCMT	d
$N_2H^{+(\alpha1)}$	5.0(−10)		-	NLTE RT Model	3	submm - JCMT	n
$SO^{(\alpha1)}$	2.0(−8)		-	NLTE RT Model	3	submm - JCMT	n
$SO_2^{(\alpha1)}$		6.0(16)	200	Absn. Depth	2	IR - ISO	m

$a(b)$ means $a \times 10^b$.
In $^{(\alpha1)}$ the first symbol denotes the fit number (α is the first fit, β is the second, ...), and the second is the component of that fit (1 is the first component, 2 is the second, ...).
The (CO) notation signifies that $T_{\rm ex}$ was forced to be one of the three CO temperatures from Mitchell et al. (1989).
Method & Weight: the method used to infer, and the significance we ascribe to, the observational result (higher is better).
[a] Lahuis & van Dishoeck (2000), [b] Boonman et al. (2001), [c] Carr et al. (1995), [d] van Dishoeck (2001, private communication), [e] van der Tak et al. (1999), [f] McCall et al. (1999), [g] Boonman et al. (2000), [h] Boonman (2001, private communication), [i] van der Tak et al. (2000), [j] Choi et al. (1994), [k] Wright (2001, private communication), [l] Goldsmith et al. (2000), [m] Keane et al. (2001), [n] van der Tak (2002, in preparation), [o] Mitchell et al. (1989).

measurements are often more useful for probing the cool exterior. These expectations are relatively consistent with the results of Table 1, where many of the absorption measurements include significant high excitation temperature components, while the inferred excitation temperatures for the emission data are generally much lower.

3. Model

In this section, a brief synopsis of the physical, thermal, and chemical models are provided. For more detailed information, see van der Tak et al. (1999, 2000), Doty & Neufeld (1997), and references therein. For reference, the model parameters are reproduced in Table 2.

3.1. Physical model

Our model for AFGL 2591 concentrates on the extended envelope of source. While an inner disk may be present, OVRO interferometric observations by van der Tak et al. (1999) suggest an unresolved central source of radius $30 < r(\mathrm{AU}) < 1000$. These and other continuum observations were analyzed by van der Tak et al. (2000) using a modified version of the self-consistent continuum radiative transfer model of Egan et al. (1988). Based upon the fit to the continuum flux and surface brightness, as well as CS line data, they constrained the density to a power law of the form $n(r) = n_0(r_0/r)^\alpha$. In particular, they found a best fit with $\alpha = 1.0$, and $n_0 \equiv n(\mathrm{H}_2, r = r_0 = 2.7 \times 10^4\ \mathrm{AU}) = 5.8 \times 10^4\ \mathrm{cm}^{-3}$. We adopt these values for the remainder of the paper. Our inner radial position was chosen to be $r_{\rm in} = 2 \times 10^2$ AU, corresponding to $T \sim 440$ K (see below). This inner radius was chosen not only for consistency with the observations of van der Tak et al. (2000), but also as extrapolation of a density power law further into the interior of the envelope leads to column densities inconsistent with observations (see Sect. 4.2 below).

Following the analyses of van der Tak et al. (1999, 2000) and Doty & Neufeld (1997), we assume that the physical and thermal model does not change significantly with time so that an equilibrium may be achieved, but we do allow for a time-dependent chemical evolution. While the collapse and rise in luminosity will occur on short time scales (<1000 yr), it is the combination of density

Table 2. Model parameters.

Parameter	Value	Ref.
Outer radius (AU)	3.0(4)	a
Inner radius (AU)	2.0(2)	a
Density $[n(r) = n_0(r_0/r)^\alpha]$		
... Exponent $[\alpha]$	1.0	a,b
... Ref. position $[r_0]$ (AU)	2.7(4)	b
... Ref. H_2 density $[n_0]$ (cm^{-3})	5.8(4)	b
CR ionization rate $[\zeta]$ (s^{-1})	5.6(−17)	c
Initial Abundance ($T > 100$ K)		
CO	3.7(−4)	a
CO_2	3.0(−5)	d
H_2O	1.5(−4)	d
H_2S	1.6(−6)	see text
N_2	7.0(−5)	e
CH_4	1.0(−7)	e
C_2H_4	8.0(−8)	e
C_2H_6	1.0(−8)	e
OI	0.0(0)	e
H_2CO	1.2(−7)	e
CH_3OH	1.0(−6)	e
S	0.0(0)	e
Fe	2.0(−8)	e
Initial Abundance ($T < 100$ K)		
CO	3.7(−4)	a
CO_2	0.0(0)	f
H_2O	0.0(0)	f
H_2S	0.0(0)	f
N_2	7.0(−5)	e
CH_4	1.0(−7)	e
C_2H_4	8.0(−8)	e
C_2H_6	1.0(−8)	e
OI	8.0(−5)	g
H_2CO	0.0(0)	f
CH_3OH	0.0(0)	f
S	6.0(−9)	see text
Fe	2.0(−8)	e

$a(b)$ means $a \times 10^b$, All abundances are gas-phase, and relative to H_2

[a] van der Tak et al. (1999), [b] van der Tak et al. (2000), [c] van der Tak & van Dishoeck (2000), [d] Boonman et al. (2000), [e] Charnley (1997), [f] assumed frozen-out or absent in cold gas-phase, [g] taken to be ∼ consistent with Meyer et al. (1998).

structure and luminosity of the central source that sets the temperature structure. Therefore, as long as the envelope mass and luminosity do not significantly change, we can consider the source as approximately constant over the $\sim 10^5$ yrs in which the envelope will be dissipated (Hollenbach et al. 1994; Richling & Yorke 1997). To see this, consider the fact that the free fall and sound-crossing times at the outer edge are both $\sim 2 \times 10^5$ yrs. While these timescales are smaller closer to the center, accretion events should probably only be important in the very interior.

Finally, we note that an outflow has been observed toward this source (see, e.g., Bally & Lada 1983; Mitchell et al. 1989). However, spectroscopy shows that nearly all submillimeter lines with the exception of CO can be assigned to the envelope as their linewidths are only ∼ few km s^{-1} (see, e.g., van der Tak et al. 1999, and recent and upcoming infrared data from TEXES by Knez et al. 2002 and Boonman et al., in preparation). Only CO has a significant fraction of the observed material in the outflow. This assignment of material to the envelope rather than the outflow is also justified a posteriori as our models are able to reproduce a good deal of the observed chemistry without the requirement of shock chemistry. Because the submillimeter lines probe high excitation gas, the lower density surrounding cloud is automatically filtered out.

3.2. Thermal model

The equilibrium gas temperature within the cloud is determined by the balance between heating and cooling. The gas heating is dominated by gas-grain collisions, and the dust temperature is determined from the self-consistent solution to the continuum radiative transfer problem as above. The Neufeld et al. (1995) cooling functions were adopted, with modifications as noted in Doty & Neufeld (1997). Furthermore, as the Neufeld et al. (1995) cooling functions were constructed assuming a singular isothermal sphere (with a commensurate $n \propto r^{-2}$ density power law), they were modified to be applicable to the r^{-1} power law adopted here. This entailed two corrections. First, the column densities had to be computed correctly at each position, rather than simply relying upon the local density. Second, the cooling functions for the tabular results were modified by a factor $[N(\alpha = 2)/N(\alpha)]^f$, where $N(\alpha) \equiv \int_{r_{\rm out}}^{r} n(r)\ {\rm d}r$ is the column density for a power law distribution $r^{-\alpha}$. Here f varies linearly with $\log(N)$ from -0.5 at $N = 10^{16}$ cm^{-2} to -1.0 at $N = 10^{21}$ cm^{-2}. We take $f = 0$ for $N < 10^{16}$ cm^{-2}, and $f = -1.0$ for $N > 10^{21}$ cm^{-2}. This factor is chosen to match the functional dependence of the cooling rate on the column density as described in Neufeld et al. (1995) for H_2O – the dominant coolant utilized in tabular form – and is consistent with the fact that the cooling rate should be inversely proportional to the column density for opaque sources. The resulting gas temperature distribution is shown in Fig. 1, and is physically similar to that of Doty & Neufeld (1997), namely that $T_{\rm gas} \sim T_{\rm dust}$, as was assumed by van der Tak et al. (1999, 2000). For comparison, models run assuming $T_{\rm gas} = T_{\rm dust}$ show no significant differences.

3.3. Chemical model

The chemical model is based upon the UMIST gas-phase chemical reaction network (Millar et al. 1997). Using this network, we construct pseudo time-dependent models of

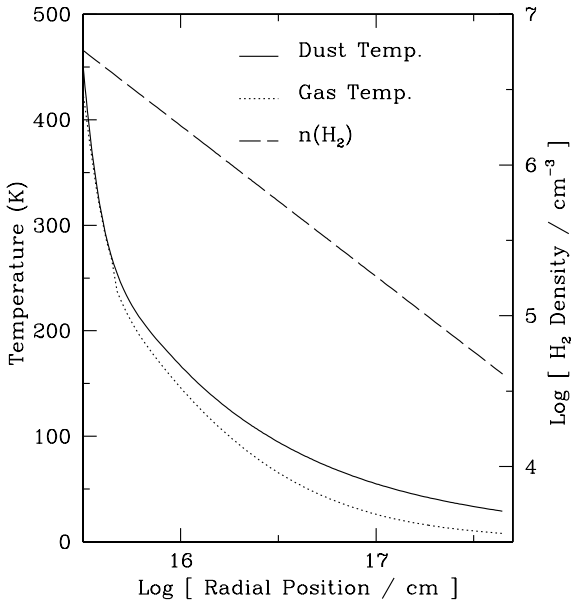

Fig. 1. Physical and thermal structure of AFGL 2591. The density and dust results from the model of van der Tak et al. (2000). The gas temperatures are calculated from the detailed thermal balance, similar to Doty & Neufeld (1997). Note that $T_{\rm gas} \sim T_{\rm dust}$.

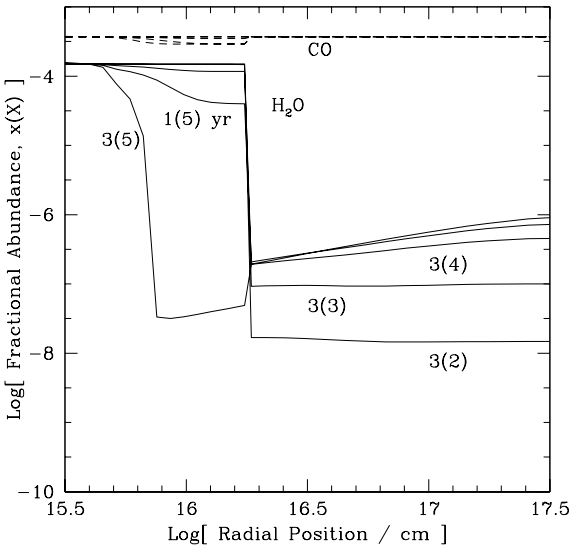

Fig. 2. The fractional abundances of CO and H_2O throughout the envelope as a function of time. The dashed-lines correspond to the (constant) CO abundance, and the solid lines to the H_2O abundance. The curves are labeled by the time in years, where $a(b) = a \times 10^b$.

the evolution of the chemical abundances. We do this over a range of 30 radial grid points, providing a time- and space-dependent chemical evolution. The local parameters (hydrogen density, temperature, and optical depth) at each radial point are taken from the physical and thermal structure calculations above. For our initial abundances, we follow Charnley (1997; private communication). These parameters allow us to reproduce many of the results of the hot core models of Charnley (1997; private communication), with most discrepancies directly attributable to differences in adopted reaction rates.

We also include the approximate effects of freeze-out onto dust grains by initially depleting certain species below 100 K (see Sect. 4.7 for discussion of H_2CO and CH_3OH). We attempt to minimize this effect by predominantly depleting those species that have high observed solid-phase abundances. Our initial fractional abundances relative to H_2, as well as other model parameters are listed in Table 2.

The cosmic-ray ionization rate is taken from van der Tak & van Dishoeck (2000) for AFGL 2591, and will be discussed in Sect. 4.5. The effects of cosmic-ray induced photochemistry were ignored. The initial sulphur abundance was chosen to make the models agree with observations (see Sect. 4.6). The assumed sulphur abundances are in general agreement with observations for both the warm (e.g., toward Orion by Minh et al. 1990), and the cold (e.g., Irvine et al. 1991) components.

The effects of photodissociation from the ISRF at the outer boundary are included, but are generally small due to the high optical depth, and the coarseness of the spatial grid considered.

4. Results

4.1. Basic molecules: H_2, CO, and H_2O

Due to their stability, CO and H_2O are significant chemical sinks, with abundances that are relatively constant with time. To see this, in Fig. 2 we plot the fractional abundance of CO and H_2O throughout the envelope as functions of time. As can be seen, the CO abundance is essentially constant in time. The abundance has been chosen to be consistent with observations.

The water abundance in the warm interior is nearly constant, due to the fact that the majority of the oxygen not in CO is initially placed into water. This is consistent with models we and others (e.g., Doty & Neufeld 1997; Charnley 1997) have run which show that even when the oxygen is not initially bound in water, nearly all of the available oxygen is converted into water on a timescale of about one hundred years due to fast neutral-neutral reactions in the warm gas.

The near discontinuity in the water abundance at $T \sim 100$ K is due to the release of water from grain mantles. This discontinuity is consistent with observations of warm ($T \sim 300{-}500$ K) water in absorption toward AFGL 2591 (Helmich et al. 1996; Boonman et al. 2000), with the lack of strong emission by cold water at long wavelengths (Boonman et al. 2000), and by detailed modeling of the line emisson to be discussed in a forthcoming paper (Boonman et al., in preparation).

As noted by Charnley (1997), the ion fraction and electron density grow with time. As seen in Fig. 2 this leads to a destruction of water on timescales of $>10^5$ years in the interior, in agreement with the results of Charnley (1997).

While the cosmic-ray ionization continually creates ions which destroy water, reformation is temperature dependent. A simple extrapolation of the "critical temperature" for water formation from Charnley (1997) for our adopted cosmic-ray ionization rate and density yields 180–200 K. Based upon the temperature structure in Fig. 1, this implies destruction of water for $r \sim 6 - 8 \times 10^{15}$ cm, in agreement with the results in Fig. 2. It should be noted that the destruction of water for $t > 10^5$ yrs is probably unimportant for AFGL 2591 based both upon the water distribution inferred by Boonman et al. (in preparation), and the chemical evolution timescale of $<10^5$ yrs discussed in Sect. 5.

Finally, the growth in the water abundance with time in the exterior occurs through slower (due to the lower abundances) ion-molecule reactions. Again, the ion-molecule reactions are driven by cosmic-ray ionization. In the exterior, average abundances of $< 3{\times}10^{-7}$ are achieved for $t \sim 3 \times 10^4$ years.

The results in Fig. 2 have interesting implications for the interpretation of water abundances. First, a simple estimate of the water abundance inferred from the model radial column densities [assuming $x(H_2O) = N(H_2O)/N(H_2)$] would suggest a fractional abundance of water in our model of $x(H_2O) \sim 3 \times 10^{-5}$. This is a factor of 5 lower than the actual water abundance adopted in the interior, and would by itself imply a significantly different structure and chemistry involved. This underscores the potential pitfalls in interpreting column densities, as well as the importance of modeling the complete physical, thermal, and chemical structure of the envelope in order to properly compare the relevant regions with observations.

A second implication is that beam dilution can have an important effect on the inferred column densities. A simulated beam-averaged column density commensurate with the beam of the Submillimeter Wave Astronomy Satellite (SWAS) would imply a water abundance of $x(H_2O) = N(H_2O)/N(H_2) = 10^{-7}$–$10^{-8}$ depending upon the time considered. This low abundance is due to significant beam-dilution from the small region of enhanced H_2O in the large beam. The range of abundances is similar to that inferred by SWAS (see e.g., Snell et al. 2000; Melnick et al. 2000; Neufeld et al. 2000). Clearly, such an observation alone does not constrain the entire envelope. While it implies that a portion of the envelope (e.g., $T \leq 100$ K) has a low water abundance, it does not restrict the potential for a compact region of significant water abundance.

As a comparison of the column densities with observations, in Fig. 3 we plot the H_2, CO, and H_2O column densities as a function of time. We assign errorbars of a factor of two consistent with the intrinsic uncertainties in the H_2O and CO results, and with the fact that the H_2 results are scaled from the CO data, as well as various radiative transfer effects. The ranges of the observed column densities are given by the shaded regions. As expected, our data match the observed column densities within the uncertainties.

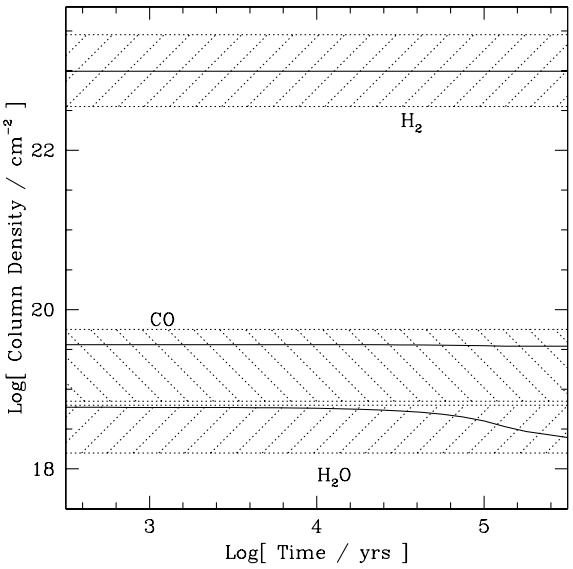

Fig. 3. The radial column densities of H_2, CO, and H_2O as function of time (solid lines). The shaded regions correspond to the observed abundances (with factor of two errorbars).

4.2. Hydrocarbon and nitrogen chemistry

Observations by Lahuis & van Dishoeck (2000) suggest that the 14 μm bands of C_2H_2 and HCN are good tracers of hot gas. Perhaps more importantly, the increase in observed column densities for temperatures above a few hundred K implies that their chemistry may be altered at high temperatures. Since all of their inferred excitation temperatures are well above the expected desorption temperature of ∼100 K, it is expected that these enhanced abundances are due to warm gas-phase chemistry.

In order to test this, we have constructed single-position models for the chemistry at $n(H_2) = 10^7$ cm^{-3} and $T \geq 200$ K. The results are shown in Fig. 4. Clearly, higher temperatures do increase the abundances of simple hydrocarbons and nitrogen-bearing species, with higher abundances prevalent once $T \sim$ few hundred K.

The enhanced HCN abundance is similar to that found by Rodgers & Charnley (2001). In parallel with their work, we find that the 756 K endothermic reaction $CN + H_2 \rightarrow$ HCN proceeds quickly for $T > 200$ K, producing significant HCN. However, while Rodgers & Charnley (2001) assume the reaction $C^+ + NH_3$ favors $HCNH^+$ (following ab initio calculations by Talbi & Herbst 1998), we assume that H_2NC^+ is the favored product to account for the observed HNC/HCN abundance ratio in many sources. In our case, then, the CN is formed via the neutral-neutral reaction $CS + N \rightarrow CN + S$. This reaction has a barrier of 1160 K, leading to significant production for temperatures above 200 K. Overcoming these barriers can increase the abundance from a peak of 10^{-8} at 200 K, to $\sim 10^{-7}$ for $t > 4 \times 10^4$ years, and $\sim 10^{-6}$ for $t > 3 \times 10^5$ years for $T \geq 400$ K.

Methane shows perhaps the most dramatic increase in abundance at very high temperatures. In fact, methane contains more carbon at the latest times than all species

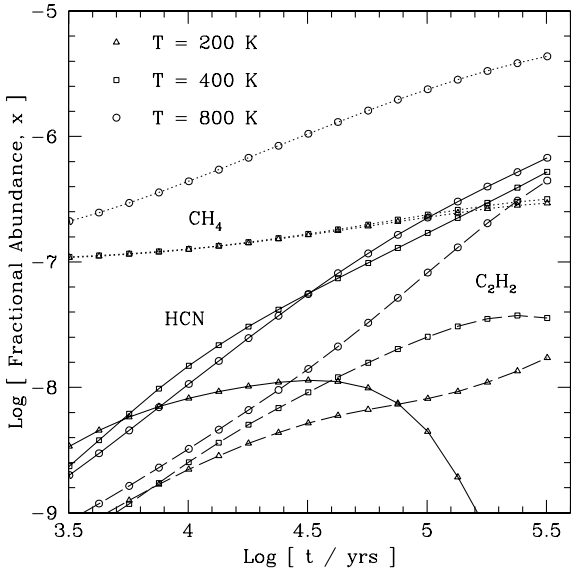

Fig. 4. The fractional abundances of HCN, CH_4, and C_2H_2 as functions of time for various temperatures. Here $n(H_2) = 10^7$ cm^{-3}. Notice the general enhancement of the abundances with increasing temperature.

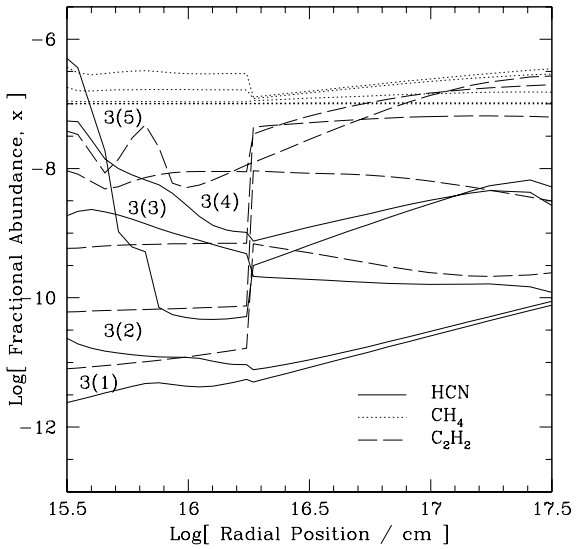

Fig. 5. The time evolution of the fractional abundances of HCN, CH_4, and C_2H_2 throughout our model, incorporating the temperature and density distributions desribed in the text. The HCN data are labeled by the time in years, where $a(b) = a \times 10^b$. The times for each curve increase upward at the inner radial position. Note the enhancement of the abundances in the warmer interior.

other than CO_2 and CO initially. This is due to the fact that ion-molecule reactions driven by cosmic-ray ionization (e.g., $He^+ + CO \rightarrow C^+ + O$) can produce C^+. This then reacts via carbon insertion (Herbst 1995) with H_2 to form CH^+ at high temperatures, and then in a chain with H_2 up to CH_3^+, which dissociatively recombines to form CH. While CH_3^+ can also dissociatively recombine to form CH_2, the dominant pathway to CH_2 at high temperatures is $CH + H_2 + 1760\ K \rightarrow CH_2 + H$. Reactions with H_2 then produce CH_4 (overcoming barriers of 6400 K and 4740 K to form CH_3 and CH_4 respectively), leading to abundances of $1 - 3 \times 10^{-7}$ for $T \leq 400$ K. However, once the temperature increases to $\sim$ 600–800 K, abundances can reach $x(CH_4) \sim 10^{-6}$ at $t \sim 3 \times 10^4$ years.

Acetylene is also enhanced at high temperatures. The pathway here is similar to that in diffuse and dark clouds (van Dishoeck & Hogerheijde 1999). However, in our model, acetylene is formed via reactions of water with $C_2H_3^+$ instead of dissociative recombination. A second difference is that $C_2H_3^+$ is produced via $C_2H_4 + H_3^+$. While the "usual" $CH_4 + C^+$ production route still occurs, the destruction of C_2H_4 by O is reduced as the temperature increases due to the fact that the oxygen is quickly converted into water by neutral-neutral reactions (see Sect. 4.1). Again, cosmic-ray ionization, carbon insertion, and water play a role, both in the production of H_3^+, and in the production of C_2H_4 via $CO \rightarrow C^+ \rightarrow \ldots \rightarrow CH_3^+ + CH_4 \rightarrow C_2H_5^+ + H_2O \rightarrow C_2H_4$. The enhanced C_2H_2 abundance is in the range $5 \times 10^{-9} \leq x(C_2H_2) \leq 2 \times 10^{-8}$ for 200 K $\leq T \leq$ 800 K at $t = 3 \times 10^4$ years. At late times, it is almost always less than 3×10^{-8} at 200 K, less than 5×10^{-8} at 400 K, and can reach 5×10^{-7} at 800 K.

In order to see how this high-temperature chemistry pertains to our model, in Fig. 5 we plot the fractional abundances of HCN, CH_4, and C_2H_2 throughout the envelope for various times. As expected from the previous discussion, we see enhanced abundances of HCN, C_2H_2, and CH_4, especially in the warm interior. The enhancement of C_2H_2 in the exterior has two primary causes. First, in this region C_2H_2 is primarily formed via dissociative recombination of $C_2H_3^+$. The destruction of $C_2H_3^+$ by O has a 215 K barrier that cannot be overcome in the cool exterior, leaving more $C_2H_3^+$ to produce acetylene. Second, an alternate production pathway via $C_3H_3^+ + O \rightarrow C_2H_2$ is enhanced in the exterior due to our increased initial O abundance in that region (see Table 2).

Cosmic-ray driven ion-molecule chemistry again plays a role for $t > 10^5$ years. In particular, the destruction of HCN near 10^{16} cm is due to reactions with HCO^+. For C_2H_2 both HCO^+ and O are important destruction reactants near 10^{16} cm. The enhancement in C_2H_2 near $r \sim 6 - 8 \times 10^{15}$ cm is due to a decrease in atomic oxygen at this position for late times (see also Sect. 4.6).

Observations of high-lying HCN lines in the submillimeter were undertaken by Boonman et al. (2001). They utilized a sophisticated radiative transfer model of the excitation, line shapes and strengths to analyze their data, and suggested that HCN follow a "jump" model, with an abundance of $x(HCN) \sim 1 \times 10^{-6}$ for $T \gtrsim 230$ K, and $x(HCN) \sim 10^{-8}$ for the cool exterior. The results in Figs. 4 and 5 are consistent with this supposition, with abundances of a few $\times 10^{-7}$ at high temperatures, and $\sim 10^{-8}$ at lower temperatures and later times.

As expected, the results in Fig. 5 are not as dramatic as in Fig. 4, as our physical and thermal model only extends into $T \sim 440$ K, less than the temperatures at which

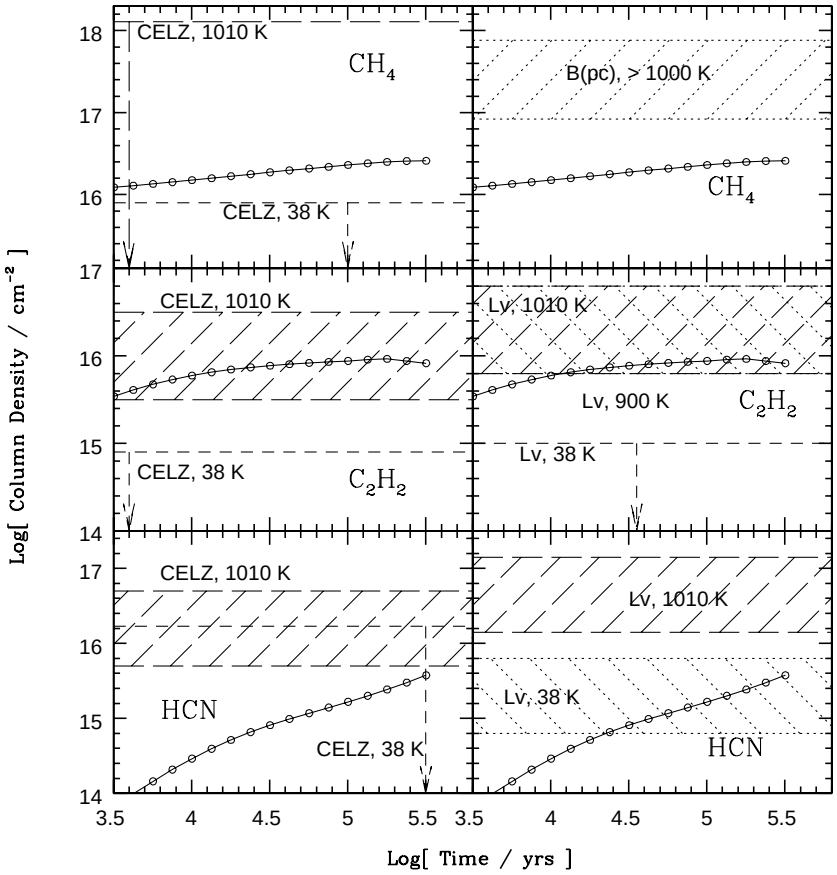

Fig. 6. A comparison of the predicted and observed column densities of HCN, CH_4, and C_2H_2 as a function of time. The model predictions are given by the solid lines and accompanied by the filled circles. The observations are divided into two groups. The left-hand panels are for the infrared data of Carr et al. (1995 CELZ), while the right-hand panels are for ISO data from Lahuis & van Dishoeck (2000 Lv) and Boonman (B(pc), private communication). Data which are upper limits are signified by downward arrows. Other data have been given an arbitrary factor of 3 uncertainty, and are given by the shaded regions.

the greatest enhancements occur. Consequently, care must be used when comparing the results with observations, as the different temperature components may not necessarily probe the portions of the region being modeled.

Such a comparison is given in Fig. 6. Here the model predictions for CH_4, C_2H_2, and HCN are compared with the infrared observational data, which probe column density. In the left-hand panels we compare to the data of Carr et al. (1995), omitting the 200 K data as these arise in the outflow. In the right-hand panels we compare to the data of Boonman (private communication), and Lahuis & van Dishoeck (2000).

When we compare with the lower temperature data, the CH_4 model results are close to the observed error bounds. On the other hand, they are well above the high temperature component of the observations. This is not a suprise, as the CH_4 chemistry is relatively unaffected below about 400 K, with very significant production at higher temperatures.

On the other hand, the C_2H_2 data fit the high temperature components of the observations. This seems to imply that while high temperature chemistry can be important, the effects are noticeably smaller than for CH_4, consistent with the results of Fig. 5. In particular, the fact that the predicted column density is so much higher than the low-temperature column density suggests that warm chemistry can enhance C_2H_2, while the fact that the predicted column densities fall in the lower range of the observed values suggests that there exists room for some enhancement ($\sim 3-5\times$) in the C_2H_2 abundance at higher temperatures, consistent with Fig. 5.

Finally, in the lower panels of Fig. 6 we show the comparison for HCN. Here we see the potential for further importance of high-temperature chemistry. In the lower-left panel, the HCN model prediction is consistent with the upper limit derived by Carr et al. (1995) at low temperatures. Similarly, in the lower-right panel, the predicted column densities are consistent with the low-temperature component fit by Lahuis & van Dishoeck (2000). In both cases, it appears that our model reproduces the production of cool HCN quite well.

On the other hand, the model predictions are well below the observed column densities for the hot components in each of the panels. This is most probably due to the significant production of HCN at temperatures above 400 K (see above). This is further supported by the fact that when a single temperature component is determined by Lahuis & van Dishoeck (2000), they find $T \sim 600$ K. Taken

at face value, their data suggest that our model does not extend inward far enough to include this hot gas.

At this point, one may ask if a simple extension of our power-law model inward would increase the temperature and column density sufficiently to fit the observed HCN data (i.e., at 1010 K). We have examined this possibility by extending our model inward, with no success. While a fractional abundance of $x(\mathrm{HCN}) \sim 10^{-7}$ would reproduce the data, the conditions necessary would also produce a water column density $N(\mathrm{H_2O}) \sim 4\times10^{19}\,\mathrm{cm^{-2}}$, over an order of magnitude above the observations.

An alternative solution is to adopt a "flattened" (i.e., $n(r) \propto r^0$) density profile for $r < r_{\mathrm{in}}$. In this case, the extra column of water would be consistent with the observations, and the column of HCN would vary as $N(\mathrm{HCN}) \sim 2 \times 10^{15}(x(\mathrm{HCN})/10^{-7})$. While the column could be fit if $x(\mathrm{HCN}) = 10^{-6}$, this is inconsistent with the results of Fig. 5. First, the chemistry does not show strong variation between 400 and 800 K, suggesting that high temperatures alone will not produce significantly more HCN. Furthermore, to achieve $x(\mathrm{HCN}) = 10^{-6}$ at these temperatures would require an extended time for chemical evolution in the interior, and would be inconsistent with the abundances of other observed species (see Sect. 5).

There are four possible resolutions to this difficulty. First, and least likely, is the possiblity that the chemical evolution time in the interior is somehow longer than in the exterior. We can think of no way in which this may occur. The second possibility is that the hydrocarbon and nitrogen chemistry is currently incomplete, especially at high temperatures. If another pathway to producing HCN exists above about 600 K, it would be possible to have abundances of 10^{-6}. Third, there is the possibility that HCN is present in grain mantles, and is injected into the hot gas. Though this is expected to be unimportant (van der Tak et al. 1999), it may conceivably play a small role.

The fourth, and perhaps most likely, possibility is that there exists some as of yet unidentified destruction mechanism for water at high temperatures. This would remove the problem of the overly-large water column if the envelope were to simply extend further inward. It is possible that evidence exists for this. As discussed by van Dishoeck (1998) observations of water gas and ice toward various sources show significantly less total water in hotter sources than in cooler sources. Given our current understanding of the chemistry of H_2O production, it would be easiest to explain this effect if there existed a mechanism for H_2O destruction at high temperatures. Further study into the high temperature chemistry of water, hydrocarbons, and nitrogen-bearing species would be of significant importance in understanding this problem.

4.3. Sulphur chemistry

The chemistry of sulphur in hot cores is well-described by Charnley (1997). In our model, we have adopted a chemistry and set of initial conditions (in the warm region) which is similar. However, given the fact that his model was for a single point in space, while our model extends over a range of physical and thermal parameters, and given recent observations of sulphur-bearing molecules toward AFGL 2591, we present our results here.

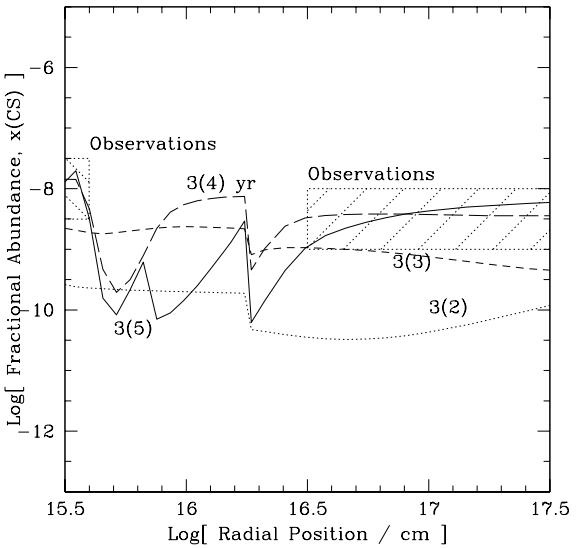

Fig. 7. The fractional abundance of CS throughout the envelope for various times. Nearly half of the sulphur is in CS at late times in the cool exterior, essentially "fixing" the gas-phase sulphur abundance. The agreement with observations in the warm interior, however is not fixed. The curves are labeled by the time in years, where $a(b) = a \times 10^b$.

In the cool exterior of our model we find that there exist a large number of pathways to shuttle sulphur into CS. The end product is that approximately 50% of the sulphur is transformed into CS by $t \sim 10^5$ years. This is shown in Fig. 7, where we plot the fractional abundance of CS for various times. No single production reaction accounts for more than 25% of the final CS abundance. This means that, at late times at least, CS is a good measure of the sulphur abundance in the exterior. To accomodate this fact, and in order to match observations of the CS abundance (see Table 1), we adjust the initial sulphur abundance to $x(\mathrm{S}) = 6 \times 10^{-9}$ for $T \leq 100$ K. This produces a nearly constant abundance in the exterior in good agreement with the observations.

In the interior, the CS abundance increases at intermediate and late times to $x(\mathrm{CS}) \sim 10^{-8}$. This is also in agreement with the observations. However, while the abundance in the exterior is essentially "forced" by our initial sulphur abundance, the fraction in CS in the interior is not.

The variation in the interior CS abundance (as with water and the hydrocarbons) is again related to the oxygen and cosmic-ray driven ion-molecule chemistry. In particular the dip near $r \sim 5 \times 10^{16}$ cm is due to the increased atomic oxygen abundance (see Sect. 4.6) in this region. This leads to more conversion of sulphur to SO_2, and thus less to CS. The decrease in CS abundance near 10^{16} cm

at $t = 1 - 3 \times 10^5$ yrs is due to the fact that there is less OH available for conversion of sulphur out of H_2S to CS.

The sulphur abundance in the warm ($T \sim 100$–400 K) gas is well-determined by the SO_2 abundance. In our model, SO_2 is formed by $H_2S + (OH, H) \rightarrow HS + O \rightarrow SO + OH \rightarrow SO_2$. The initial reactions of H_2S with H and OH have barriers of 352 K and 80 K, respectively. As a result, little SO_2 is produced in the cool exterior, while the barriers can be overcome in the interior leading to significant SO_2 production. As the temperature further increases, however, the OH can be more easily forced into water, leaving little for the $SO + OH \rightarrow SO_2 + H$ reaction. This can be seen in the very interior of Fig. 8, where the SO_2 abundance drops at high temperatures. In our model approximately 90% of the sulphur returns to atomic form at ∼440 K, with approximately 10% in H_2CS, and a few percent in CS and OCS.

While we are are unable to identify the sulphur reservoir assuming solar abundances roughly hold, it appears that a significant portion would need to exist in or on dust grains. Under this constraint, we can also identify SO_2 as the primary sink of molecular sulphur in warm (100–300 K) gas (assuming no O_2 is released during heating of the grain mantles – Charnley 1997). As a result, the sulphur abundance in warm molecular gas at later times can be approximately determined by the SO_2 abundance. In our model, this requires the adjustment of the initial H_2S abundance from the value of 10^{-7} adopted by Charnley (1997) to 1.6×10^{-6}. This value is, coincidentally, similar to the H_2S gas-phase abundance seen by Minh et al. (1990) toward Orion. A comparison of our model predictions with observations by Keane et al. (2001) show similar column densities of 4×10^{16} cm^{-2} and 6×10^{16} cm^{-2} respectively. It is also intruiging that the excitation temperature inferred by Keane et al. (2001) for SO_2 toward AFGL 2591 is ∼750 K, suggesting formation in a warm dense region of a few hundred K.

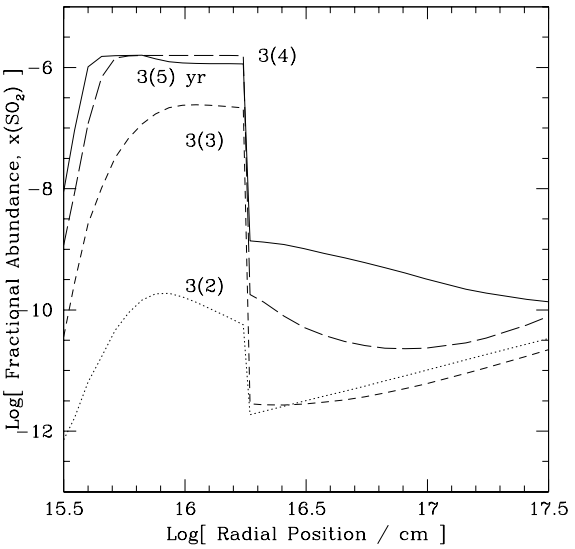

Fig. 8. The fractional abundance of SO_2 throughout the envelope at various times. Note the increase near $T = 100$ K as the free sulphur is forced into SO_2. The decrease at high temperatures is due to the loss of the reactant OH via its more efficient inclusion into water at those temperatures. The curves are labeled by the time in years, where $a(b) = a \times 10^b$.

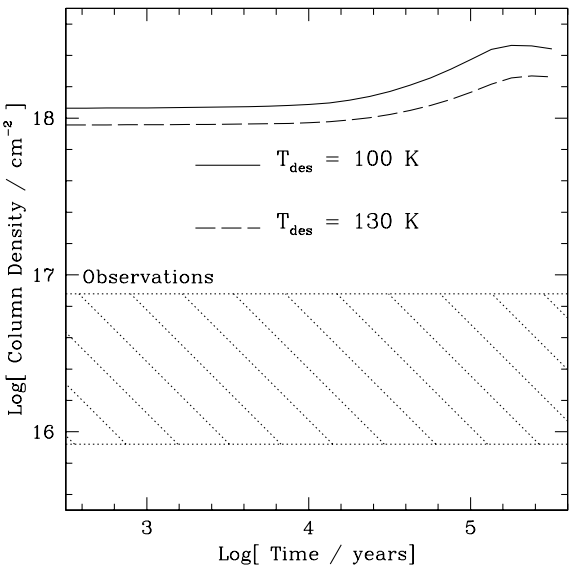

Fig. 9. The column density of CO_2 predicted by our base model as a function of time (solid and dashed lines) for two different assumed desorption temperatures. No impulsive heating event is assumed (see text). The observed column is shown by the shaded region. Notice the extent to which the model overpredicts CO_2.

4.4. CO_2 chemistry: Potential heating events?

An important problem in the chemistry of the envelopes of massive young stars is the low observed gas-phase abundance of CO_2 (see e.g., van Dishoeck & van der Tak 2000). Observations by ISO indicate large solid CO_2 abundances (de Graauw et al. 1996; Whittet et al. 1998; Ehrenfreund et al. 1998; Gerakines et al. 1999), with a CO_2/H_2O abundance in the ice mantles of 10–20%. In the warm regions close to the protostars, these mantles should be evaporated. Assuming water ice abundances of a few $\times 10^{-5}$ (Tielens et al. 1991; Gensheimer et al. 1996) implies a liberated fractional abundance of $x(CO_2) \sim 10^{-5}$–10^{-6}. On the other hand, ISO observations of gas-phase CO_2 (van Dishoeck et al. 1996; Boonman et al. 2000) suggest $x(CO_2) \sim 10^{-7}$. These results indicate that CO_2 is quickly destroyed after evaporation from ice mantles.

To see this discrepancy between the amount of CO_2 predicted in our base model and that observed, in Fig. 9 we plot the predicted CO_2 column density as a function of time. Also plotted are the observations of Boonman et al. (2000). Clearly, the base model significantly overpredicts the CO_2 column density in AFGL 2591, confirming the general results above.

Charnley & Kaufman (2000) studied destruction of CO_2 by both H and H_2, suggesting that destruction of CO_2 by H in postshock flows could be important. In order

to test this, we have constructed models with non-zero atomic hydrogen abundances, as would be expected in partially dissociative shocks. While the CO_2 can be effectively destroyed on a shock cooling timescale of ∼30 yrs, CH_4, NH_3, and H_2O can be destroyed even more efficiently. While this does not pose a significant problem for CO_2 or NH_3 which have low observed abundances or upper limits, there are effects on other species. In particular, in dissociative shocks the water column density is decreased by a factor of 2–3. Furthermore, once destroyed, only little water is re-formed in the range $100 \leq T(\mathrm{K}) \leq 300$, inconsistent with the results of Boonman et al. (in preparation). Similarly, the O and O_2 abundances are significantly increased. On the other hand, the CH_4 abundance is decreased by an order of magnitude in the interior. This process only requires a few percent H_2 dissociation.

A second potential difficulty is that it is unclear if a large enough fraction of the envelope can be disturbed by a shock to significantly affect the global CO_2 abundance, as evidenced by the relatively small line-widths in much of the envelope (van der Tak et al. 1999).

Doty et al. (2002) reconsidered this problem in light of previously unused laboratory measurements of the destruction of CO_2 by H_2 (Graven & Long 1954). They found that destruction by H_2 may dominate destruction by H in the very warm gas, near $T \sim 1000{-}1600$ K. While this may occur in a number of ways, Doty et al. (2002) considered two possibilities: a uniform temperature increase (such as from the passage of a $v \sim 20{-}30$ km s^{-1} MHD shock – Draine et al. 1983), and a central luminosity increase caused, for example, by an accretion (FU-Orionis-type) event. The possibility of impulsive heating events may be supported by evidence from continuum emission by crystalline silictes (Smith et al. 2000; Aitken et al. 1988) which suggests that an annealing event may have occurred in AFGL 2591. If such a heating event occurred, Doty et al. (2002) find that it is possible for the CO_2 to be removed on a timescale of 10^0–10^4 years by H_2. Recent calculations of the potential surface for the $CO_2 + H_2$ reaction suggest, however, that the barrier for the reaction may be higher than indicated by the old laboratory experiments, so that this issue remains unsettled (Talbi & Herbst 2002). Clearly, further laboratory studies of this reaction at high temperatures are urgently needed.

While speculative, destruction of CO_2 by H_2 in this fashion has some advantages. First, there is very little atomic hydrogen available to affect the chemistry, and in particular to influence CH_4, O, O_2, and H_2O. Second, and perhaps more importantly, variations in the observed column density of CO_2 may potentially be explained by variations in the size and/or duration of the proposed heating event – depending upon its origin, or the time since the heating event and the local cosmic-ray ionization rate.

As a final note, it is interesting to also consider the possibility that the CO_2 desorption temperature may be greater than 100 K. Recent work by Fraser et al. (2001), suggests that the desorption temperature of water may be as high as 120–130 K. If the solid CO_2 is contained in a water-ice matrix as suggested by observations (Gerakines et al. 1999), then it may be interesting to consider the effect of this higher desorption temperature on $N(CO_2)$. In Fig. 9, we present predicted column densities for the re-formation of CO_2, assuming desorption temperatures of both 100 K and 130 K. The effect is a decrease in the CO_2 column densities by a factor of two, insufficient to explain the discrepancies.

4.5. Cosmic-ray ionization rate

As discussed earlier, cosmic-ray ionization can play an important role in driving ion-molecule chemistry at later times. In our model, we adopt the cosmic-ray ionization rate for AFGL 2591 of $\zeta = 5.6 \times 10^{-17}$ s^{-1} as determined by van der Tak & van Dishoeck (2000). While the cosmic ray flux is unique, the ionization rate will vary with position if the particles are absorbed. As evidence for cosmic ray absorption is inconclusive (see, e.g., van der Tak 2002), we adopt a single cosmic ray ionization rate for AFGL 2591.

In Fig. 10 we plot the predicted fractional abundance of HCO^+ and N_2H^+. There are two important features. First, there is significant destruction of HCO^+ at the water desorption position, due to the reaction $HCO^+ + H_2O \rightarrow H_3O^+ + CO$. This is in agreement with the model of van der Tak & van Dishoeck (2000). While they argue that this jump in abundances is not important in constraining the cosmic ray ionization rate, our overall HCO^+ abundance is consistent with their observations, and thus lends support to their somewhat high value for ζ in AFGL 2591. The situation is similar for N_2H^+. Second, at $t = 3 \times 10^5$ yrs, the ion abundances increase in the interior. This is consistent with Charnley (1997), and is due to the fact that the cosmic-ray ionization continues to produce more ions, which eventually destroy a significant fraction of the complex molecules up to the position where the temperature is high enough to re-form them.

The cosmic-ray ionization rate also affects the abundance of H_3^+. In our models, reasonable time ($t \geq 10^3$ years) column densities are $\sim 5 \times 10^{14}$ cm^{-2}, almost a factor of 5 below those observed by McCall et al. (1999). If a comparison of these results were used to infer a cosmic-ray ionization rate, one would obtain a much larger value. While large H_3^+ abundances in the diffuse ISM have been reported by McCall et al. (2002) – which they suggest may be due to uncertainties in dissociative recombination rate – van der Tak & van Dishoeck (2000) have also noted that there exists a variation in H_3^+ column density with distance which suggests that intervening clouds may be important.

The cosmic-ray ionization rate also affects the HCN abundance. Decreasing ζ makes it harder to form HCN. For example lowering ζ by a factor of three decreases the enhancement of HCN by a factor of three even at 800 K, placing the warm HCN abundance at $\leq 3 \times 10^{-7}$ – well below the observations. Furthermore,

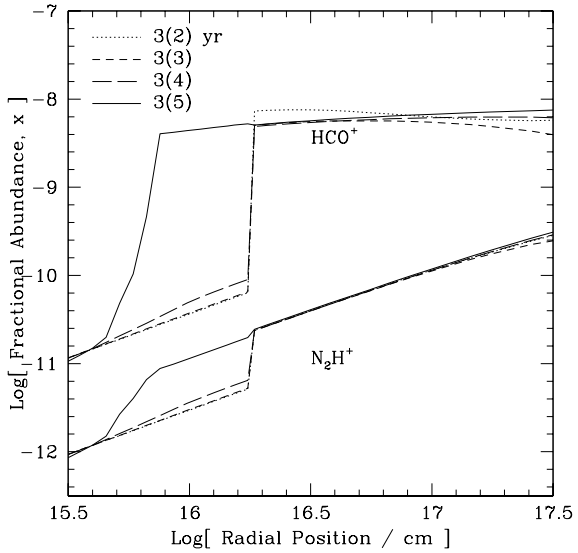

Fig. 10. The fractional abundance of HCO^+ and N_2H^+ througout the envelope for various times. Note the marked decrease about 100 K, where reactions with H_2O become important. The curves are labeled by the time in years, where $a(b) = a \times 10^b$.

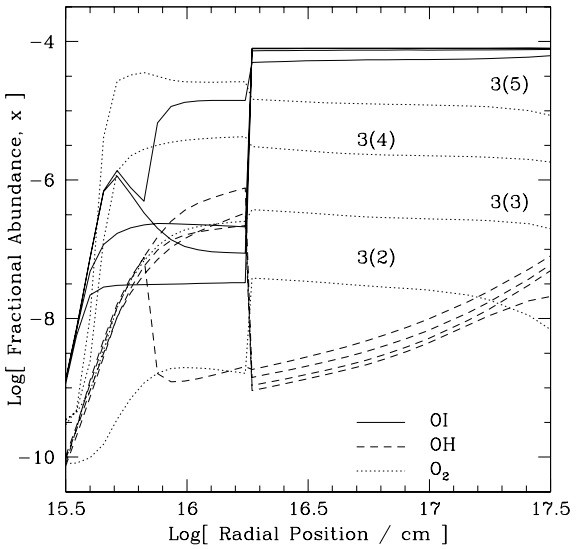

Fig. 11. The fractional abundance of O, OH, and O_2 throughout the envelope for various times. The curves are labeled by the time in years, where $a(b) = a \times 10^b$. The times increase upward. The only exception is the dip for OH near 10^{16} cm, which corresponds to $t = 3 \times 10^5$ yrs.

the same change also increases the time for the cold column of HCN to reach the observed range to $t \sim 10^5$ yrs, in disagreement with the age constraints discussed below in Sect. 5.

Based upon these results, it appears that the value of $\zeta = 5.6 \times 10^{-17}$ s^{-1} inferred by van der Tak & van Dishoeck (2000) is correct to within a factor of three. Any value much lower would significantly hamper the production of HCN, making for disagreement with the observations. Any value much higher would be in conflict with the observed ion abundances.

4.6. Other species

As oxygen and oxygen-bearing species can have a significant effect on the chemistry, in Fig. 11 we plot the fractional abundances of O, OH, and O_2 as functions of position for various times.

The increase in the atomic oxygen abundance near 10^{16} cm is due to the fact that O is freed from water at late times via ion-molecule reactions with H_2O and CO as discussed in Sect. 4.1. As the water is destroyed, the main production mechanism for OH [$(HCO^+, \ H_3^+) + H_2O \rightarrow H_3O^+ + e^- \rightarrow$ OH] is removed. This leads to a decreased OH abundance at this position at late times.

The peak in the atomic oxygen abundance near $r \sim 5{-}8 \times 10^{15}$ cm is due to the competition between production of O by ion-molecule reactions with CO, and the destruction of O at high temperatures by reactions with OH and H_2. Once the temperature reaches ∼180–200 K, neutral-neutral re-formation of water can balance the destruction by ion-molecule reactions on these timescales, as discussed in Sect. 4.1, and in Fig. 2. This leads to a greater OH abundance at these positions, and thus a decreased O abundance.

In any case, the excess atomic oxygen is easily converted to molecular oxygen over time at temperatures less than 300 K. This places an important constraint on the temporal evolution of the source as discussed in Sect. 5 below.

It is also interesting to note that the dominant nitrogen resevoir is molecular nitrogen. While atomic nitrogen is somewhat abundant (see Table 3), only about 1% or less of the nitrogen is in atomic form – and that preferentially at later times.

Although we have endeavored to consider detailed comparisons between our model predictions and observations, a worthwhile test of any model is the predictions it makes for future observations. Consequently, in Table 3, we give predicted radial and beam-averaged column densities at $t = 3 \times 10^4$ yrs for various species with $N > 10^{13}$ cm^{-2}. The beam-averaged column densities assume a Gaussian beam of full-width at half-max of 15 arcsec, though the results are insensitive to this assumption.

4.7. Implications for mantles and mantle destruction

Finally, although we do not explicitly consider grain-surface chemistry, it is worthwhile to discuss the implications our results have on the grain mantles, and grain-surface chemistry. Two observed species that may form on grain mantles are H_2CO and CH_3OH. In Fig. 12 we plot the fractional abundance of H_2CO and CH_3OH throughout the envelope at various times.

When low-temperature depletion is assumed, the column densities for H_2CO and CH_3OH are generally close to the observations. In particular, while van der Tak et al. (2000) report column densities of $N(H_2CO) = 8 \times 10^{13}$ cm^{-2} and $N(CH_3OH) = 1.2 \times 10^{15}$ cm^{-2}

Table 3. Predicted column densities at $t = 3 \times 10^4$ yrs.

Species	$N_{\rm radial}$(X)	$N_{\rm beam}$(X) – 15″
OI	4(18)	3(18)
N	3(16)	2(16)
S	1(16)	7(13)
NO	1(16)	5(15)
OH	9(15)	1(15)
SO	4(15)	2(13)
H_2CS	2(15)	1(13)
C_3H	2(15)	2(15)
C_4H	1(15)	1(15)
C_3H_2	7(14)	7(14)
CH_3OCH_3	6(14)	7(12)
CHOOH	4(14)	1(14)
NH_2	3(14)	2(13)
CH_2CO	2(14)	2(14)
CH_3	2(14)	6(12)
NH	1(14)	3(12)
H_3O^+	8(13)	2(13)
CN	5(13)	5(13)
OCN	5(13)	1(13)
NS	5(13)	9(10)
C_2S	4(13)	3(13)
HS_2	4(13)	1(12)
C_6H	4(13)	4(13)
C_3H_3	3(13)	2(13)
CCN	3(13)	3(13)
H_2C_3	3(13)	2(13)
$CH_3OH_2^+$	2(13)	2(11)
HNO	2(13)	1(13)
CH_3CHO	2(13)	7(12)

$a(b)$ means $a \times 10^b$.
All column densities given in $\rm cm^{-2}$.

respectively, the model predicts a CH_3OH column density about 6 times lower, and an H_2CO column density about 5 times higher.

On the other hand, detailed radiative transfer modeling by van der Tak et al. (2000) suggests that the observed lines are consistent with a uniform H_2CO abundance of 4×10^{-9}, and a CH_3OH abundance of 2.6×10^{-9} for $T \leq 100$ K, and 8×10^{-8} for $T \geq 100$ K. For comparison the predicted abundances for these species are shown in Fig. 12. The H_2CO abundance in the cool exterior is consistent with the inferred abundance, while the abundance in the warm interior is predicted to be significantly higher and decreases only slowly with time. The CH_3OH, on the other hand, does not fit the inferred abundances very well. While there does exist a "jump" as suggested by van der Tak et al. (2000), the abundances predicted by the model are significantly too low in the exterior and too high in the interior.

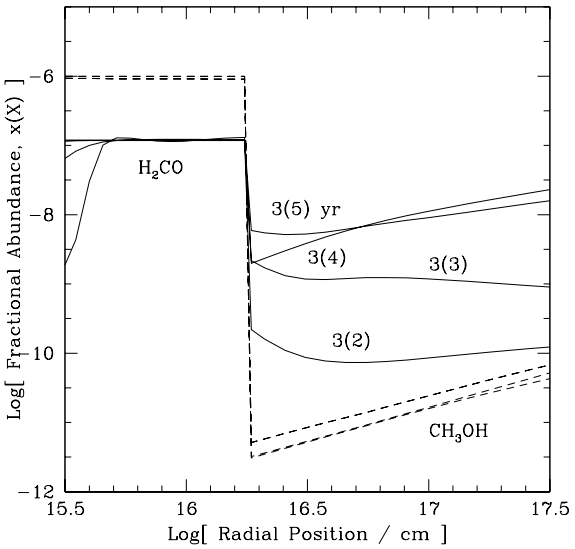

Fig. 12. The fractional abundance of H_2CO and CH_3OH throughout the envelope for various times. The curves are labeled by the time in years, where $a(b) = a \times 10^b$. Note that both species are initially depleted from the gas phase for $T \leq 100$ K.

For comparison, we have also run models where the abundances of H_2CO and CH_3OH are initially undepleted for $T \leq 100$ K. In models where the cold initial abundances of CH_3OH are set equal to the hot initial abundances only CH_3OH, C_3H_3, and CH_3OCH_3 show column density differences of a factor of three or more. When we adopt this initial abundance, the column density of CH_3OH increases to 4.4×10^{15} $\rm cm^{-2}$, a value approximately 4 times larger than the observations. These results suggest that while we can reproduce the CH_3OH column density with some accuracy, simple gas-phase chemistry alone cannot reproduce the apparent details of the CH_3OH abundance distribution. As a result, it appears that CH_3OH can be strongly affected by grain surface chemistry, also in the cooler regions.

Allowing a cold H_2CO abundance equal to the warm abundance changes the predicted column density by only a factor of two, with only minor differences for all other species. This implies that only observations of high-enough spatial resolution to differentiate between the warm and cold phases, or use of high-excitation lines will be able to best determine the nature of H_2CO formation.

It is also interesting to consider the fact that submillimeter observations suggest that the abundances of warm H_2CO and CH_3OH are factors of 100–1000 below the solid state abundances. In our models, we find that the ratio of warm to cold H_2CO for a 15 arcsec beam is $60 \leq [N(H_2CO)]_{T \geq 100}/[N(H_2CO)]_{T \leq 100} \leq 500$ for $3 \times 10^4 \leq t(\rm yrs) \leq 10^5$. On the other hand, for CH_3OH we find that $1 \leq [N(CH_3OH)]_{T \geq 100}/[N(CH_3OH)]_{T \leq 100} \leq 2$ for $3 \times 10^4 \leq t(\rm yrs) \leq 10^5$. This confirms the previous suggestions that that gas-phase chemistry may perhaps dominate grain-surface chemistry in the production of H_2CO, while there must be some other (presumeably grain-surface) pathway to the production of CH_3OH.

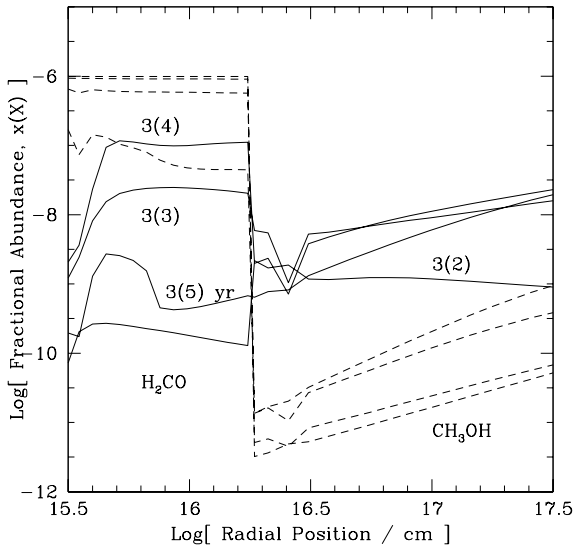

Fig. 13. The fractional abundance of H_2CO and CH_3OH throughout the envelope for various times, after a hypothetical non H_2-dissociative heating event. The curves are labeled by the time in years, where $a(b) = a \times 10^b$. Note that both species are initially depleted from the gas phase for $T \leq 100$ K.

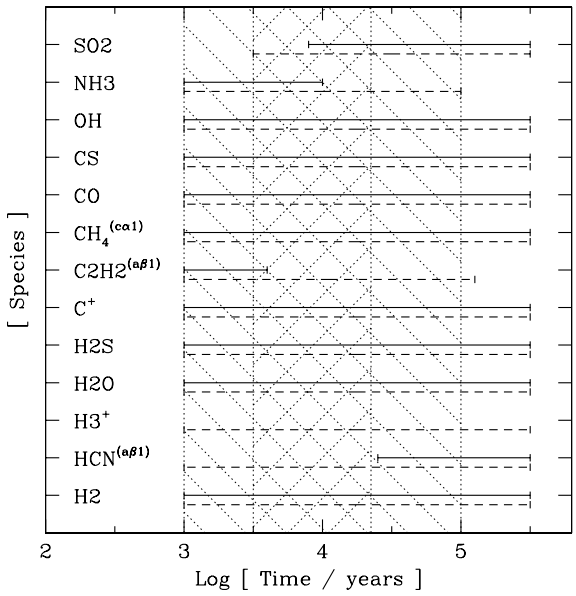

Fig. 14. A comparison of the predicted and observed abundances and column densities for the species listed in Table 1, and observed in the infrared (see text). The solid lines correspond to agreement between the models and observations within a factor of 3, and the dashed-lines to within a factor of 10. The species are listed, with notes on the observational fits given as parentheses as in Table 1. The two shaded regions denote the regions of potential and preferred fit between the model and the observations (see text). Notice the agreement with Fig. 15.

As a final note, we have considered the effect of a heating event (as proposed in Sect. 4.4) in which H_2 is not dissociated on the H_2CO and CH_3OH chemistry. The results are shown in Fig. 13. As can be seen, the later-time abundances are more consisent with the results inferred by van der Tak et al. (2000). In particular, the CH_3OH abundance in the interior is in the range of $5\times10^{-8} \leq x(CH_3OH) \leq 6\times10^{-7}$, while in the exterior the abundances can reach as high as $0.3 - 1 \times 10^{-9}$. Likewise, the H_2CO abundance for $3 \times 10^4 \leq t(\mathrm{yrs}) \leq 3 \times 10^5$ is in the range $10^{-7} \geq x(H_2CO) \geq 3 \times 10^{-10}$. While not conclusive, this brackets the inferred H_2CO abundance of 4×10^{-9} nicely. If further suggestions of a heating event are found, it may be useful to re-visit these data for comparison with observations as they may provide a gas-phase mechanism for the production of H_2CO and CH_3OH.

5. Time constraints

Based upon the large amount of observational data for AFGL 2591 (see Table 1), and given the time-dependent nature of the reaction network, one important test of the physical and chemical model would be a determination of the chemical evolution time of the envelope, consistent with all or most of the observed species. This has been proposed and carried out previously (e.g., Stahler 1984; Millar 1990; Helmich et al. 1994; Hatchell et al. 1998) in single-point models of dense cloud cores, with some success.

In our case, we determine the time-dependent fractional abundances and column densities for each of the species observed in Table 1. As discussed in Sect. 2.3, we divide the data into two sets: those for which infrared absorption measurements have been made, and those for which submillimeter emission measurements have been made.

In Figs. 14 and 15 we plot the approximate time ranges over which the listed species match the observed data. In both figures, the solid lines represent agreement to within a factor of 3, while the dashed lines represent agreement to within a factor of 10. These limits can be considered good and acceptable levels of agreement respectively (see e.g., Millar & Freeman 1984, and Brown & Charnley 1990). In both figures, the lower limits to the chemical evolution time are capped at 10^3 years. As in Table 1, observational data are appended to each species name. We include all species from Table 1, except for CO_2. As discussed in Sect. 4.4, there are significant discrepancies and questions about the gas-phase chemistry of CO_2, and as such we have treated it separately in that section. For species other than CO_2, we include the data that is relevant to comparison with our model (i.e., the most reliable components).

In Fig. 14, we can see a wide variation of possible times when constraining the models by the infrared data. We place two limits on the evolution: a wide range of $10^3 \leq t(\mathrm{yrs}) \leq 1\times10^5$, and a preferred limit of $3\times10^3 \leq t(\mathrm{yrs}) \leq 2.5 \times 10^4$. These regions are identified by the shading in Fig. 14.

For comparison, in Fig. 15 we plot the constraints on the time for the submillimeter data. As discussed in Sect. 2.3, results based upon sophisticated, self-consistent, radiative transfer modeling are given slightly more weight,

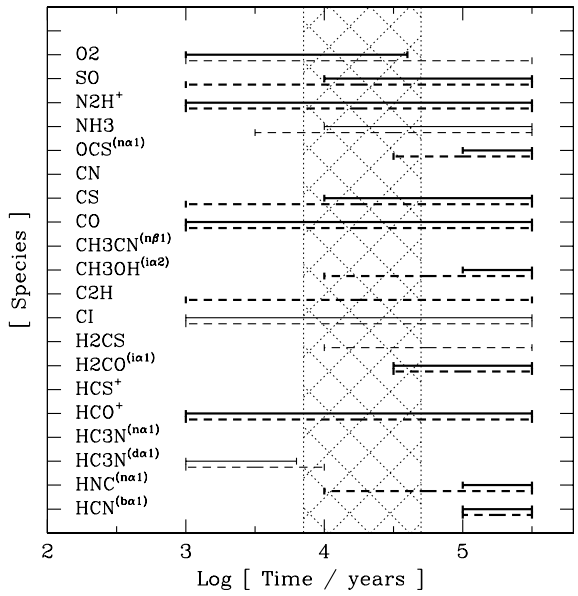

Fig. 15. A comparison of the predicted and observed abundances and column densities for the species listed in Table 1, and observed in the submillimeter (see text). The solid lines correspond to agreement between the models and observations within a factor of 3, and the dashed-lines to within a factor of 10 (see text for details). The species are listed, with notes on the observational fits given as parentheses as in Table 1. The shaded region denote the regions of preferred fit between the model and the observations. Notice the agreement with Fig. 14.

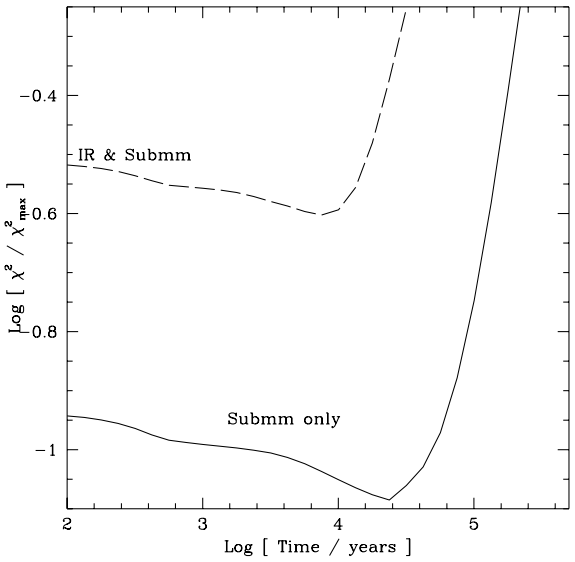

Fig. 16. The quality of the model fit to the observations as a function of time. Here we plot the χ^2 as defined in the text, normalized to the maximum value for the times considered. The solid line shows the chi-squared for the submillimeter data only, while the dashed-line shows the results when both the submillimeter and infrared data are included.

and identified by the bold lines in Fig. 15. Also, the O_2 upper limit by SWAS is given more weight. This is done because in the absence of upper limits for the O_2 abundance toward AFGL 2591 in particular, we have used the largest quoted upper limit of $N(O_2)/N(H_2) \leq 9 \times 10^{-7}$ (Goldsmith et al. 2000). Where radiative-transfer modeling derived abundances are not available, we have calculated the appropriate beam-averaged column densities for comparison with the observations.

Most species in Fig. 15 fit the models to within an order of magnitude of the observational data. Those that do not fit are not significant defects, for a number of reasons. First, not all data are in disagreement with the models – both OCS and HC_3N have other observations / reductions which do agree with the models. Second, the discrepancies can be understood on a case-by-case basis. For instance, the chemistry and reaction rates of OCS are only poorly understood at best (Millar, private communication). It is interesting to note, however, that the radial OCS column density matches the observed column density. Also, we expect the potential difficulties with species related to HCN (such as HC_3N and CH_3CN) as our model does not probe the complete region over which significant HCN production may be important (see Sect. 4.2 above). In the case of HCS^+, the abundance is strongly affected by enhancements of CS abundance at temperatures of 10–20 K (Helmich 1996), lower than all but our outermost temperature, signifying that the AFGL 2591 envelope may be more extended than we have assumed. In a similar fashion, CN is strongly influenced by UV radiation from a PDR (Helmich 1996), a radiation source not considered in our model.

The age-constraints implied by the results in Fig. 15 suggest chemical evolution times in the range $7 \times 10^3 \leq t(\mathrm{yrs}) \leq 5 \times 10^4$, with a strong preference for $t \sim 3 \times 10^4$ years. These constraints are shown by the shaded region in the figure.

In order to attempt to quantify this result, in Fig. 16 we plot the chi-squared value between the models and the observations, normalized to the maximum chi-squared in the entire time evolution. The χ^2 is defined by $\chi^2 \equiv \Sigma_i w_i^2 \times [y_{\mathrm{model},i} - y_{\mathrm{obs},i}]^2/\sigma_i^2$. Here we include the weight from Table 1 as w, and assume uncertainties of a factor of 5 in the observations for all species except O_2, for which we assume a factor of 2 uncertainty as we already have adopted the highest observed upper limit from Goldsmith et al. (2000). These results are generally consistent with those of Figs. 14 and 15, both in terms of the preferred times as well as the relatively lower level of constraint provided by the IR data. In particular, while times of up to $\sim 10^5$ yrs may be possible, there appears to be a preference for somewhat lower times near $\sim 3 \times 10^4$ yrs.

It is interesting and reassuring that the chemical evolution times from both the infrared and submillimeter data provide similar results. This is especially true as they probe such different regions of the envelope. Also, the nearly simultaneous agreement in time between such different species, with transitions arising throughout the envelope, and observed with a range of ground- and space-based instruments provides significant support to the proposed chemical, physical, and thermal structure of the envelope.

6. Conclusions

We have constructed detailed thermal and gas-phase chemical models for AFGL 2591 based upon the physical model of van der Tak et al. (1999, 2000). These models were used to probe the validity of the proposed physical structure, as well as study the chemical evolution of the source.

In particular, we find that:

1. Pseudo-time dependent modeling of the chemistry as a function of depth is a good probe of the physical and thermal structure of the source, due to the density and temperature dependence of the chemistry.
2. Care must be exercised when drawing conclusions from observations, as infrared absorption measurements usually better probe the warm interior of the envelope while submillimeter emission data often better probe the cool exterior. While "average abundances" [$x_{\rm avg} \equiv N({\rm X})/N({\rm H_2})$] can suggest conditions different from those actually in existence, detailed radiative transfer modeling are essential to give more reliable results (Sects. 2 and 4.1). This also underscores the importance of modeling the complete physical, thermal and chemical structure of the envelope when comparing to observations.
3. Water and CO are stable, even at high temperatures, except for destruction by cosmic-ray-driven ion-molecule reactions for $t > 10^5$ yrs. The ice and gas abundances toward other sources suggest that there may exist a water destruction mechanism at high temperatures (>500 K). Such a mechanism does not exist in our chemical model, but is worth further exploration (Sects. 4.1 and 4.2).
4. The hydrocarbon and nitrogen chemistry is strongly influenced by temperature, with significant production possible at high ($T \geq 400$ K) temperatures. Still it appears that there may exist an as-yet unexplored path to HCN for $T \geq 600$ K (Sect. 4.2).
5. The sulphur chemistry displays three significant regimes. In the cool exterior, over 50% of the sulphur exists in CS. For $100 \leq T({\rm K}) < 300$, SO_2 contains a majority of the sulphur. At higher temperatures, atomic sulphur dominates. While consistent with observations, these results employ a low gas-phase sulphur abundance. We cannot identify the principle sulphur reservoir in the cold gas (Sect. 4.3).
6. Carbon dioxide may possibly be destroyed by reactions with molecular hydrogen in impulsive heating events – a reaction which requires further study. The suggestion that CO_2 may be destroyed by H has problems in that it may destroy too much CH_4 in the interior and produce too much atomic and molecular oxygen (Sect. 4.4).
7. The cosmic-ray ionization rate in AFGL 2591 is important. It affects the ion abundances as well as the formation of HCN. These processes fix the cosmic ray ionization rate to better than a factor of three. Ions produced by cosmic rays can also effectively destroy H_2O on timescales of $>10^5$ years (Sect. 4.5).
8. We produce simulated column densities of predicted abundant species for comparison with future observations (Table 3). We predict, among other things, abundant atomic oxygen and nitrogen – even though oxygen can be shuttled to water and O_2 while nitrogen is at most 1% atomic with the majority in N_2. The temperature variation within the source can have a large affect on oxygen, and hence on the rest of the chemistry (Sect. 4.6).
9. While it is possible for the observed H_2CO abundance to be reproduced by gas-phase chemistry, the same is not true for CH_3OH. This suggests that some other processes are important for CH_3OH, including grain-surface chemistry and/or the potential of a heating event within the envelope (Sect. 4.7).
10. It is possible to use detailed chemical modeling to constrain the chemical age of AFGL 2591. We find $7 \times 10^3 \leq t({\rm yrs}) \leq 5 \times 10^4$, with a strong preference for $t \sim 3 \times 10^4$ years (Sect. 5).
11. The agreement of our results with the line data lend significant further confirmation to the physical model proposed by van der Tak et al. (2000), and the chemical structure and evolution proposed here.

Acknowledgements. We are grateful to the anonymous referee for comments and discussions that helped improve the presentation. This work was partially supported under grants from The Research Corporation (SDD), and the Netherlands Organisation for Scientific Research (NWO) through grant 614-41-003 (AB, FvdT), and a NWO bezoekersbeurs. Astrochemistry at Leiden is supported through an NWO Spinoza award (EvD).

References

Aitken, D. K., Roche, P. F., Smith, C. H., et al. 1988, MNRAS, 230, 629
Bally, J., & Lada, C. J. 1983, ApJ, 265, 824
Bergin, E. A., Langer, W. D., & Goldsmith, P. F. 1995, ApJ, 441, 222
Beuther, H., Schilke, P., Menten, K., et al. 2002, ApJ, 566, 945
Boonman, A. M. S., et al. 2001, ApJ, 553, L63
Boonman, A. M. S., et al. 2000, in ISO beyond the peaks, ed. A. Salama, M. F. Kessler, K. Leech, & B. Schulz, ESA-SP 456, 67 [astro-ph/0105249]
Brown, P. D., & Charnley, S. B. 1990, MNRAS, 244, 432
Carr, J. S., Evans, N. J., Lacy, J. H., & Zhou, S. 1995, ApJ, 450, 667
Charnley, S. B. 1997, ApJ, 481, 396
Charnley, S. B., & Kaufman, M. J. 2000, ApJ, 529, L111
Choi, M., Evans, N. J., Jaffe, D. T., & Walker, C. 1994, ApJ, 435, 734
Churchwell, E. B. 1993, in ASP Conf. Ser., 35, Massive Stars, Their Lives in the Interstellar Medium, ed. J. P. Cassinelli, & E. B. Churchwell, ASP, 35
Churchwell, E. B. 1999, in The Physics of Star Formation and Early Stellar Evolution II, ed. C. J. Lada, & N. D. Kylafis (Kluwer), 515
de Graauw, T., et al. 1996, A&A, 315, L345

Doty, S. D., & Neufeld, D. A. 1997, ApJ, 489, 122
Doty, S. D., van Dishoeck, E. F., van der Tak, F. F. S., et al. 2002, A&A, submitted
Draine, B. T., Roberge, W. G., & Dalgarno, A. 1983, ApJ, 264, 485
Egan, M. P., Leung, C. M., & Spagna, G. R. Jr. 1988, Comput. Phys. Commun., 48, 271
Ehrenfreund, P., Dartois, E., Demyk, K., & D'Hendecourt, L. 1998, A&A, 339, L17
Fraser, H. J., Collings, M. P., McCoustra, M. R. S., & Williams, D. A. 2001, MNRAS, 327, 1165
Garay, G., & Lizano, S. 1999, PASP, 111, 1049
Gensheimer, P. D., Mauersberger, R., & Wilson, T. L. 1996, A&A, 314, 281
Gerakines, P., Whittet, D. C. B., Ehrenfreund, P., et al. 1999, ApJ, 522, 357
Goldsmith, P. F., Melnick, G. J., Bergin, E. A., et al. 2000, ApJ, 539, L123
Graven, W. M., & Long, F. J. 1954, J. Am. Chem. Soc., 76, 2602
Gwenlan, C., Ruffle, D. P., Viti, S., et al. 2000, A&A, 354, 1127
Hatchell, J., et al. 1998, A&A, 338, 713
Hatchell, J., Fuller, G. A., Miller, T. J., Tompson, M. A., & Macdonald, G. H. 2000, A&A, 357, 637
Helmich, F. P. 1996, Ph.D. Thesis, Leiden University
Helmich, F., Jansen, D. J., de Graauw, Th., Groesbeck, T. D., & van Dishoeck, E. F. 1994, A&A, 283, 626
Helmich, F., van Dishoeck, E. F., Black, J. H., et al. 1996, A&A, 315, L173
Herbst, E. 1995, in ASSL Vol. 202: The Diffuse Interstellar Bands, 307
Herbst, E., & Klemperer, W. 1973, ApJ, 185, 505
Hollenbach, D., Johnstone, J., Lizano, S., & Shu, F. 1994, ApJ, 428, 654
Irvine, W. M., Ohishi, M., & Kaifu, N. 1991, Icarus, 91, 2
Keane, J. V., Boonman, A. M. S., Tielens, A. G. G. M., & van Dishoeck, E. F. 2001, A&A, 376, L5
Knez, C., et al. 2002, AAS, 134.10
Kurtz, S., Cesaroni, R., Churchwell, E., Hofner, P., & Walmsley, M. 2000, in Protostars and Planets IV, ed. V. Manning, A. Boss, & S. Russel (Univ. of Arizona Press), 299
Lada, C. J., Thronson, H. A. Jr., Smith, H. A., et al. 1984, ApJ, 286, 302
Lahuis, F., & van Dishoeck, E. F. 2000, A&A, 355, 699
Leung, C. M., Herbst, E., & Huebner, W. F. 1984, ApJS, 56, 231
McCall, B. J., Hinkle, K. H., Geballe, T. R., et al. 2002, ApJ, 567, 391
McCall, B. J., Geballe, T. R., Hinkle, K. H., & Oka, T. 1999, ApJ, 522, 338
Melnick, G. A., Ashby, M. L. N., Plume, R., et al. 2000, ApJ, 539, L87
Meyer, D. M., Jura, M., & Cardelli, J. A. 1998, ApJ, 493, 222
Millar, T. J. 1990, In Molecular Astrophysics: A Volume Honoring Alexander Dalgarno, ed. T. W. Harquist (Cambridge, Cambridge University Press), 114
Millar, T. J. 1993, in Dust and Chemistry in Astronomy, ed. T. J. Millar, & D. A. Williams (IOP Publishing, Bristol), 249
Millar, T., Farquhar, P., & Willacy, K. 1997, A&AS, 121, 193
Millar, T. J., & Freeman, A. 1984, MNRAS, 207, 405
Minh, Y. C., Irvine, W. M., McGonagle, D., & Ziurys, L. M. 1990, ApJ, 360, 136
Mitchell, G. F., Curry, C., Maillard, J., & Allen, M. 1989, ApJ, 341, 1020
Neufeld, D. A., Ashby, M. L. N., Bergin, E. A., et al. 2000, ApJ, 539, L111
Neufeld, D. A., Lepp, S., & Melnick, G. J. 1995, ApJS, 100, 132
Prasad, S. S., & Huntres, W. T. Jr. 1980, ApJS, 43, 1
Richling, S., & Yorke, H. W. 1997, A&A, 327, 317
Rodgers, S. D., & Charnley, S. B. 2001, ApJ, 546, 324
Smith, C. H., et al. 2000, MNRAS, 312, 327
Snell, R. L., Howe, J. E., Ashby, M. L. N., et al. 2000, ApJ, 539, L101
Stahler, S. W. 1984, ApJ, 281, 209
Talbi, D., & Herbst, E. 2002, A&A, in press
Talbi, D., & Herbst, E. 1998, A&A, 333, 1007
Tielens, A. G. G. M., Tokunaga, A. T., Geballe, T. R., & Baas, F. 1991, ApJ, 381, 181
van der Tak, F. F. S. 2002, in Hot Star Workshop III: The Earliest Phases of Massive Star Birth, ed. P. A. Crowther, ASP Conf. Ser., in press
van der Tak, F. F. S., & van Dishoeck, E. F. 2000, A&A, 358, L79
van der Tak, F. F. S., et al. 1999, ApJ, 522, 991
van der Tak, F. F. S., et al. 2000, ApJ, 537, 283
van der Tak, F. F. S., van Dishoeck, E. F., & Caselli, P. 2000, A&A, 327
van Dishoeck, E. F. 1998, Faraday Discuss., 109, 31
van Dishoeck, E. F., & Hogerheijde, M. R. 1999, in The Origins of Stars and Planetary Systems, ed. C. J. Lada, & N. Kylafis (Kluwer), 97
van Dishoeck, E. F., & van der Tak, F. F. S. 2000, in Astrochemistry: From Molecular Clouds to Planetary Systems, IAU Symposium 197, ed. Y. C. Minh, & E. F. van Dishoeck, p. 97
van Dishoeck, E. F., et al. 1996, A&A, 315, L349
Walmsley, C. M., & Schilke, P. 1992, in Astrochemistry of Cosmic Phenomena, IAU Symposium 150, ed. P. D. Singh (Kluwer), p. 251
Whittet, D. C. B., et al. 1998, ApJ, 498, L159
Xie, T., Allen, M., & Langer, W. D. 1995, ApJ, 440, 674